International Communications in Heat and Mass Transfer 158 (2024) 107866

Contents lists available at ScienceDirect

International Communications in Heat and Mass Transfer

journal homepage: www.elsevier.com/locate/ichmt

Lagrangian CFD modeling of ammonia sprays: A correlation across flash boiling and evaporative conditions

J. Zembi [a], M. Battistoni [a,*], A. Pandal [b], R. Pelé [c], P. Brequigny [c], C. Hespel [c], C. Mounaïm-Rousselle [c]

[a] University of Perugia, Department of Engineering, 06123 Perugia, Italy
[b] University of Oviedo, Dpto. Energía, 33202 Gijón, Asturias, Spain
[c] University of Orleans, NSA-CVL, EA 4229—PRISME, 45072 Orléans, France

ARTICLE INFO

Keywords:
Ammonia spray
Flash boiling model
Droplet size data
Lagrangian spray
Atomization model
CFD

ABSTRACT

Simulations of liquid ammonia spray are performed for different ambient pressures to investigate the transition between flash-boiling and non-flashing regimes, through Computational Fluid Dynamics (CFD). The Lagrangian particle method, within the Reynolds Averaged Navier Stokes (RANS) approach for turbulence is used. Numerical results are compared with experimental liquid and vapor tip penetrations, spray morphology and Sauter Mean Diameter (SMD) measurements, for a multi-hole injector. An adaptation of Kelvin-Helmholtz - Rayleigh-Taylor (KH-RT) breakup model constants and prescribed jet cone angle is necessary for each regime, as standard values used for traditional fuels, e.g., gasoline, appear not to work with ammonia. Capturing local spray details and SMD values across all regimes with a single model setup is very challenging, especially with a new fuel such as ammonia, whose properties differ by a large amount from more established values for hydrocarbons. In this study a correlation for ammonia is proposed for the KH-RT breakup model constants and jet cone angle as a function of operating conditions across flash-boiling and non-flashing regimes. In addition, local temperature predictions are extensively discussed, for both liquid and gaseous phases, highlighting and quantifying the strong cooling effect that ammonia produces during the phase change process.

1. Introduction

Necessary measures must be adopted to mitigate climate change, and undoubtedly solutions will be related to renewable energy sources, such as solar, wind, or hydroelectric power, and to carbon neutrality in the energy and transportation sectors. Regarding the latter, considering internal combustion engines and especially long-range transportation, research efforts are directed towards the use of CO_2-free energy sources or CO_2-neutral fuels to make the green revolution possible for a zero-emission mobility. Recently, green hydrogen energy has attracted considerable attention [1], nevertheless, its transportation and safe storage at reasonable costs are extremely challenging [2], for some undesired properties such as extremely low ignition energy, low volumetric energy density, and wide flammability range [3]. In this scenario ammonia (NH_3) is a valuable alternative and an efficient hydrogen carrier [4,5], as not only does it contain a large amount of hydrogen in the molecule, but, when liquified, ammonia also provides a higher volumetric energy density and is safer to handle and store compared to pure hydrogen [6].

Ammonia as a chemical is already largely produced by industry. The main use has been in agriculture as fertilizer for a very long time. Other applications regard its usage as a refrigerant gas, for the purification of water supplies, and in the manufacture of plastics, explosives, textiles, pesticides, dyes, and other chemicals. Recently, in the context of energy transition, ammonia is extensively being studied and tested for direct usage in internal combustion engines (ICE) [7], and also as a fuel for stationary gas turbines and burners [4,5]. For the thermal applications, injection of liquid ammonia is very attractive, because of lower costs, favorable local air/ammonia mixture properties, local decrease of temperature which limits thermal NOx.

However, its use as a carbon-free fuel is a new area of interest, and a large amount of research has still to be carried out. Considering that ammonia can be easily liquefied at room temperature with relatively low pressures, in the context of gasoline direct injection (GDI) engines scientific efforts are conducted to explore the possibility of using ammonia spray as a replacement for traditional hydrocarbon fuel

* Corresponding author.
E-mail address: michele.battistoni@unipg.it (M. Battistoni).

https://doi.org/10.1016/j.icheatmasstransfer.2024.107866

Available online 27 July 2024

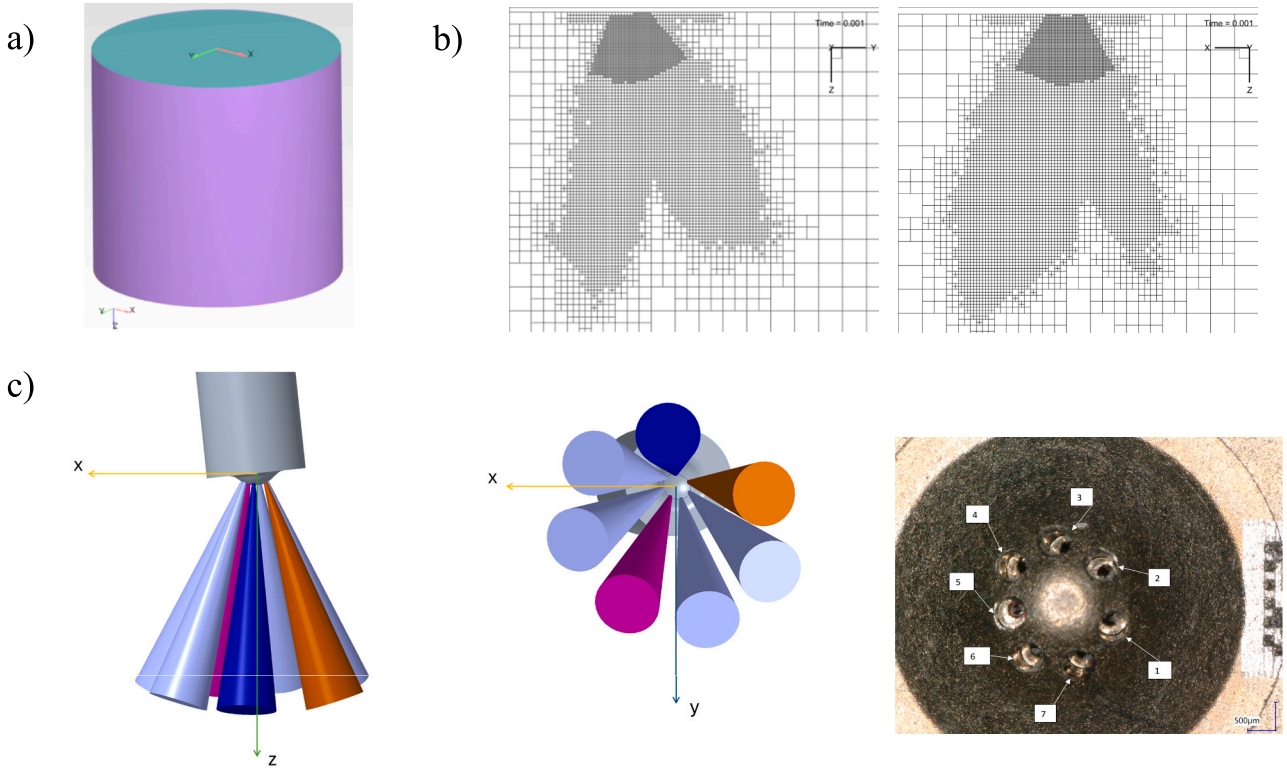

Fig. 1. Computational domain 100 mm long by 100 mm in diameter (a), mesh views in the near field (b), and nozzle geometry details (c).

injection. This scenario poses significant challenges, including the combustion process, emissions, performance, and the safe use of such a fuel. Compared to gasoline, ammonia presents different combustion characteristics. Firstly, due to its lower energy density than gasoline, a higher quantity of ammonia must be injected to achieve the same power output. Secondly, ammonia presents low ignitability and combustion stability caused by low flame speed [8]. Additionally, although it is carbon-free fuel, high nitrogen oxide (NOx) emissions [9–11] should be minimized by means of proper control of the combustion process and through aftertreatment devices, while maintaining engine performance and ensuring efficient engine operation.

The aforementioned reasons suggest that modifications to the fuel injection system, the chamber design, and the overall engine management are required. GDI injectors play a crucial role in the combustion process by precisely atomizing the fuel and injecting it directly into the combustion chamber. Hence, adopting ammonia as fuel demands a deep understanding of its atomization development, droplet size distribution, and spray formation, where each process has its own specific characteristics. In this regard, liquid ammonia is characterized by a higher vapor pressure than most other typical fuels, such as gasoline or ethanol, and flash boiling phenomena can occur very easily.

Indeed, flash boiling happens when a high-pressure subcooled liquid is injected into a low-pressure environment below its saturation pressure [12]. The process leads to very fast atomization and fuel vaporization [13]. It is therefore important to understand in detail how liquid ammonia behaves when it undergoes flash boiling in GDI injectors, to determine precisely the impact on spray formation, vaporization, and subsequent combustion. This entails investigating the whole flash boiling process, i.e., the occurrence of internal and external flashing. The former takes place inside the nozzle holes and the spray exiting the orifice turns out to be a two-phase flow composed of liquid and vapor [14]. The latter occurs directly in the combustion chamber with rapid fuel vaporization [15].

Experimental measurements are needed to gain insight and to provide fundamental knowledge on processes that occur during the spray formation. Recently, some experimental studies have been carried out in the case of ammonia [16–18]. However, experimental techniques have their own limitations that limit the extent to which the flow can be characterized. Current sophisticated engines also require the use of computational tools to be optimized and achieve further improvements. Therefore, CFD models must be informed to properly reproduce the air-fuel mixing characteristics of ammonia sprays under direct injection (DI) conditions, taking simultaneously into account atomization and flash boiling phenomena, which are clearly different from those experienced by conventional fuels [19].

Although in recent years fully Eulerian modeling approaches have shown great potentials in the simulation of direct injection fuel sprays [20–24], the most common approach within the engine research community relies on the Lagrangian particle tracking, especially for full in-cylinder simulations, to minimize the computational cost. This kind of modeling approach treats the liquid phase using a Lagrangian reference frame and the gaseous phase using an Eulerian reference frame. As widely used, there are countless models for drag, collision, breakup, and vaporization based on assumptions of nearly spherical droplets. Despite the excellent performance exhibited by these Lagrangian-based sub-models for common fluids, their effectiveness is ambiguous when liquid ammonia is considered. The typical set of model constants must be changed [25–27]. However, a thorough investigation aiming to understand these models' applicability to all ammonia spray evaporating conditions, across both flash and non-flash boiling regimes, must be done.

Specifically focusing on thermally driven flash atomization models, several attempts are present in the literature. Price et al. [28] implemented a diameter reduction factor using Riznic and Ishii's nucleation model [29] to estimate vapor flow rate and liquid droplet diameter, considering only aerodynamic breakup. Duronio et al. [30] included a thermal atomization mechanism, proposing an effervescent breakup model that postulates the presence and growth of one bubble per

Table 1
Details of nozzle orifices.

	Orifice center [mm]			Unit vector (direction)		
	x_0	y_0	z_0	u	v	w
Jet 1	−0.7069	0.0012	0.7660	−0.3115	0.0666	0.9479
Jet 2	−0.7760	0.7445	0.6325	−0.3689	0.3406	0.8648
Jet 3	−0.1762	1.1912	0.5485	−0.1316	0.4951	0.8588
Jet 4	0.5759	1.0327	0.5727	0.1627	0.4168	0.8943
Jet 5	1.0497	0.4361	0.6774	0.3665	0.1883	0.9112
Jet 6	0.9042	−0.2905	0.8091	0.3327	−0.0916	0.9386
Jet 7	0.1951	−0.5545	0.8608	0.0522	−0.1574	0.9861

droplet. Angelilli et al. [31] combined classical nucleation theory with Rayleigh-Plesset bubble growth to predict child droplet size and observed that this regime is significant only in a narrow temperature range. Shin and Park [32] used surplus energy and bubble growth rate theory to calculate spray velocity changes due to flash breakup, finding it much faster than aerodynamic breakup. However, none of these flash atomization models have been explicitly validated against ammonia spray measurements.

In addition to that, despite their complexities, all models still lack multiple additional physical aspects. Collectively, Kitamura et al. [33], Sher et al. [34], Lamanna et al. [35], and Xi et al. [36] noted how flash boiling regimes depend significantly on nozzle length-to-diameter ratio and on surface finish. All these aspects are not considered in current CFD Lagrangian flash atomization models, to the best of our knowledge.

The main contribution of the present work is addressing such aspects, in order to fill the knowledge gap on ammonia Lagrangian spray models, proposing novel correlations for atomization by taking a holistic approach. In the following, numerical CFD simulations of liquid ammonia spray have been first conducted and validated against experiments reported by Pelé et al. [18]. Correlations for ammonia are developed and proposed for the KH-RT breakup model constants and jet cone angle as a function of the operating conditions measured by the ratio between the fuel saturation pressure and the ambient pressure. The assessment of the main spray parameters is performed with the aim of building a predictive and reliable Lagrangian model for ammonia jets. Liquid and vapor tip penetration, local values of Sauter Mean Diameter and global spray morphology measurements are considered for comprehensive validation. Last, predicted liquid and gaseous local temperatures are extensively discussed as an additional distinctive feature of ammonia sprays.

2. Material and methods

2.1. Numerical setup and injector details

The Eulerian-Lagrangian two-phase flow approach is adopted, with appropriate source terms for heat, mass and momentum exchanges. For the gas phase, the compressible set of Reynolds-averaged Navier-Stokes equations is solved using the finite volume method with collocated variables. The PISO (Pressure Implicit with Splitting of Operators) algorithm is used to solve the coupling between mass and momentum via a pressure Eq. [37]. Governing equations are discretized with a second-order scheme for convection terms and with a first order implicit scheme for time integration. Simulations were run with the CFD software CONVERGE v3.0, a code widely used for two-phase flows and combustion [37–39].

Fig. 1.a shows the computational domain represented by a cylindrical vessel, while Fig. 1.b shows details of mesh in the vicinity of the nozzle. The mesh is generated on-the-fly using a Cartesian orthogonal grid and a cut-cell method at the boundaries. A base mesh size of 4.0 mm is selected and then a combination of adaptive and prescribed mesh refinements are used to reach the finest resolution of 0.25 mm in the near-nozzle region, which is in line with many other Eulerian-Lagrangian spray simulations [40–42]. It is noted that such geometry does not include the internal nozzle region, and the mesh resolution is therefore far from the typical values of Eulerian simulations intended to resolve the in-nozzle and near-exit region [43]. The present mesh construction is the result of a thorough grid independence analysis conducted in a previous work [27] in which refinement parameters were properly assessed. Turbulence is modeled, within the RANS approach, using the standard k-ε model with a modified value of $C_{\varepsilon 1} = 1.55$ [27]. A comprehensive assessment of the turbulence model impact on the spray behavior has been previously conducted in [27].

Fig. 1.c displays spray plume geometrical previews and a picture of the injector tip. The injector is a current Bosch GDI with 7 holes of 150 μm diameter, and 360 μm counterbore. Orifice center coordinates and nominal jet dictions are also listed in Table 1. Preliminary assessments of the main CFD parameters and grid independence analyses were carried out in a previous work [27].

As mentioned, the Lagrangian particle method [44] is used to simulate the dispersed liquid phase. Ammonia spray parcels are introduced in the computational domain, paying attention to achieving discretization-independent results [45]. The pressurized liquid fuel is introduced in the computational domain using the blob model, i.e., as large drops (blobs) with a diameter comparable to the size of the nozzle hole. The initial parcel diameters are determined by considering the nozzle hole diameter d_0 reduced by means of an area contraction coefficient. Then, breakup phenomena occur as parcels travels through the domain, based on the competition between Kelvin-Helmholtz and Rayleigh-Taylor (KH-RT) models.

The KH breakup occurs because of velocity difference across the gas-liquid interface. In this model the subsequent droplet dimensions are determined by assuming that the radius of the detaching droplet r_c is proportional to the wavelength of the fastest growing unstable surface wave Λ_{KH}

$$r_c = B_0\,\Lambda_{KH} \tag{1}$$

where B_0 is the size model constant. The change in drop radius r_p of a parent parcel is expressed as follows

$$\frac{dr_p}{dt} = -\frac{(r_p - r_c)}{\tau_{KH}} \tag{2}$$

$$\tau_{KH} = \frac{3.726\,B_1\,r_p}{\Lambda_{KH}\,\Omega_{KH}} \tag{3}$$

where τ_{KH} is the breakup time scale, and B_1 is the corresponding time constant of the model. The wavelength Λ_{KH} and the corresponding growth rate Ω_{KH} are calculated according to Reitz and Bracco [46].

RT instability is also considered as a contributing factor for droplet breakup. The occurrence of unstable RT waves is attributed to the rapid deceleration of the drops induced by the drag force. The fastest growing wavelength for the RT instabilities is expressed as follows

$$\Lambda_{RT} = 2\pi\sqrt{\frac{3\sigma}{a(\rho_l - \rho_g)}} \tag{4}$$

where σ is the surface tension of the droplet, a is the droplet deceleration and ρ_g and ρ_l are the gas and liquid densities, respectively. If the scaled wavelength is smaller than the droplet diameter, it is assumed that RT waves are growing on the droplet surface. The radius of the child droplets is given by

$$r_c = \Lambda_{RT} C_{RT}/2 \tag{5}$$

The RT breakup occurs when the RT waves have been growing for a sufficient time, greater than the breakup time

$$\tau_{RT} = C_I/\Omega_{RT} \tag{6}$$

Here, Ω_{RT} is the RT wavelength growth rate, while C_{RT} and

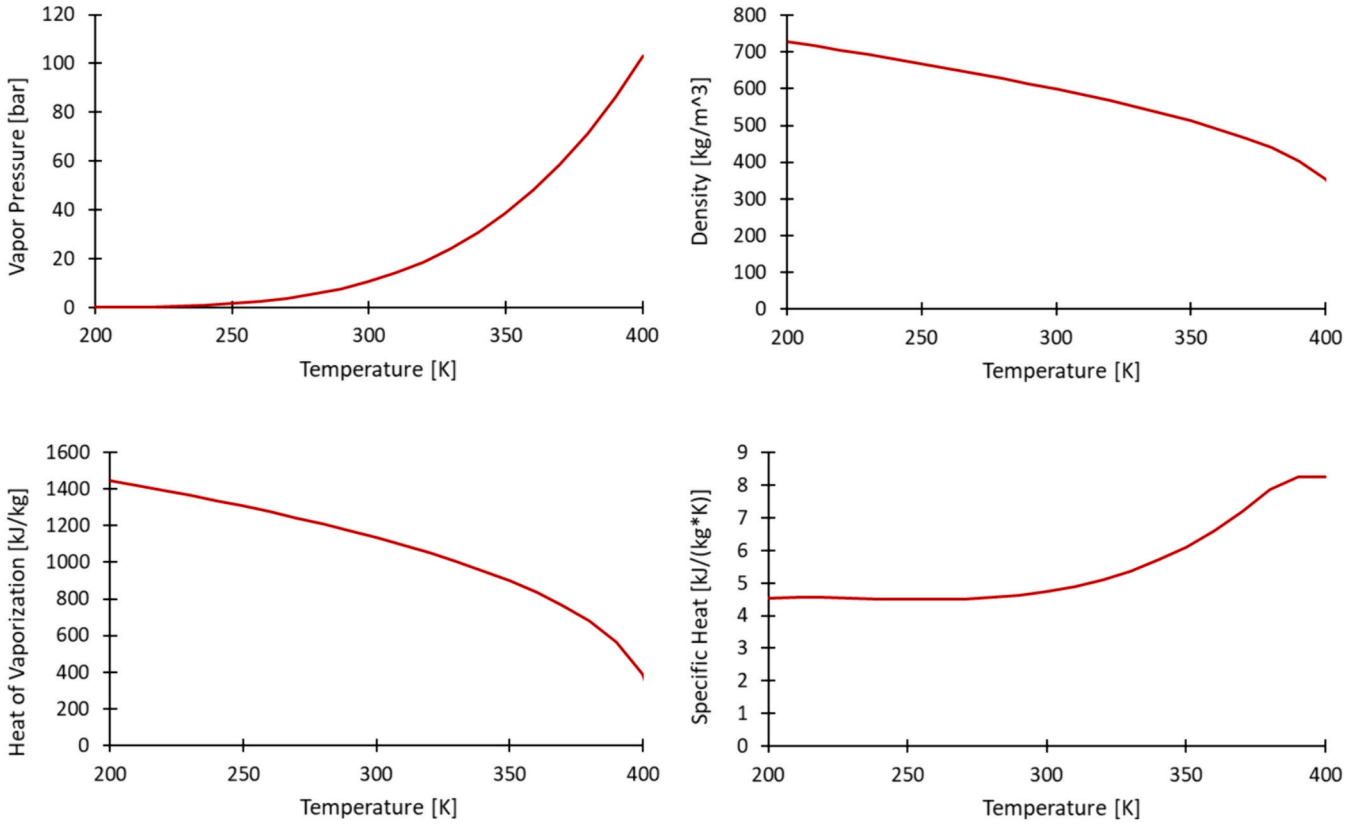

Fig. 2. Ammonia liquid properties as a function of temperature.

Table 2
Specifications of ammonia spray initial conditions.

Condition	T_{fuel} [K]	T_a [K]	ρ_a [kg/m^3]	P_a [bar]	$R_p = P_v(T_{fuel})/P_a$
1	293	293	17.82	15	0.571
2	293	293	11.88	10	0.857
3	293	293	8.32	7	1.224
4	293	293	4.76	4	2.143
5	293	293	2.38	2	4.285

$C_l$represent the size and time constants of the RT breakup model, respectively, evaluated according to Su et al. [47].

In the present work, the KH parameters are kept constant for all cases (KH time constant, $B_1 = 17.5$, KH size constant, $B_0 = 1.75$), while RT parameters are calibrated for each case and specific correlations have been developed for them (as shown in the next section).

This choice is based on the following consideration. Both models predict the growth of unstable waves in a competing manner. If the RT mechanism can break-up the droplet, then a sudden disintegration will occur. If not, the KH mechanism is responsible for continuous production of child droplets and diameter reduction of the parent drop. For this reason, priority is given to the calibration of the RT model parameters.

Besides, additional sub-models are needed to take into account other physical processes, like droplet-turbulence interaction and droplet-droplet collision. For droplet turbulence dispersion the O'Rourke model [48] is used. Transport equations for the turbulent kinetic energy of the gas phase and its dissipation include source terms to account for the depletion of turbulent kinetic energy due to work done by turbulent eddies to disperse the liquid spray droplets [38,48]. Regarding droplet-to-droplet interaction the no-time-counter (NTC) collision model [49] is included. The method introduces random sub-sampling of the parcels within each cell, to speed-up collision calculations, while maintaining

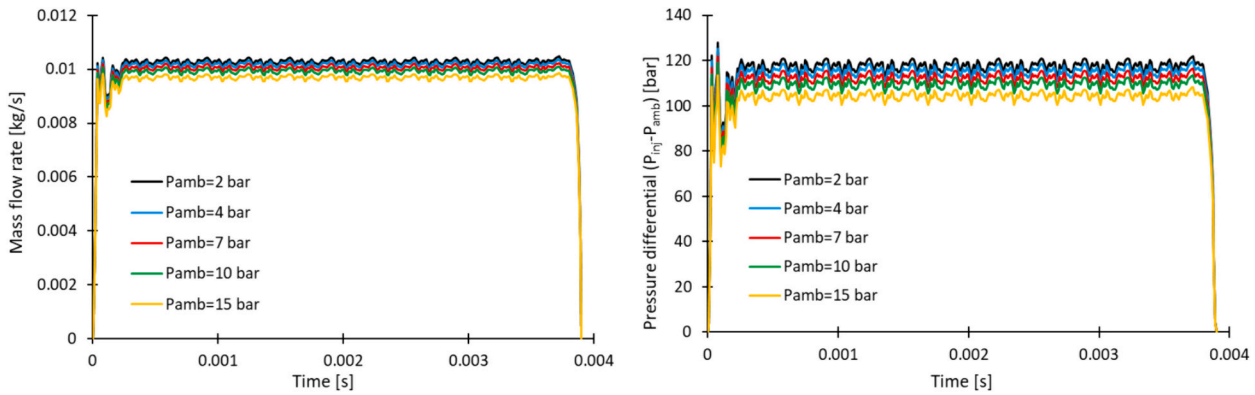

Fig. 3. Rate of injection and injection pressure difference for each ambient pressure condition.

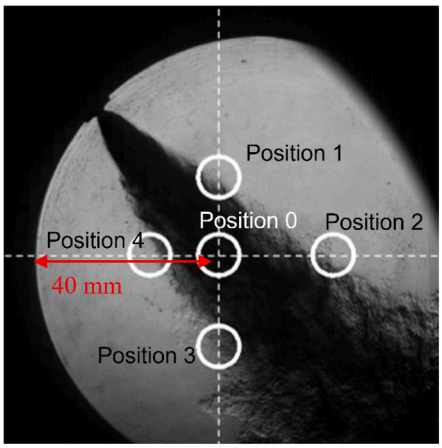

(a)

position	2 bar	4 bar	7 bar	10 bar	15 bar
	R_p = 4.285	R_p = 2.143	R_p = 1.224	R_p = 0.857	R_p = 0.571
0	8.6	14.4	20.4	26.3	33.6
1	8.5	12.6	17.7	22.2	30.3
2	12.0	18.5	26.9	31.5	39.2
3	11.5	17.2	28.6	37.7	48.5
4	8.4	14.5	15.8	28.2	41.0

(b)

Fig. 4. Measurement positions of the droplet size (a), and SMD values in [μm] (b), from [26,27].

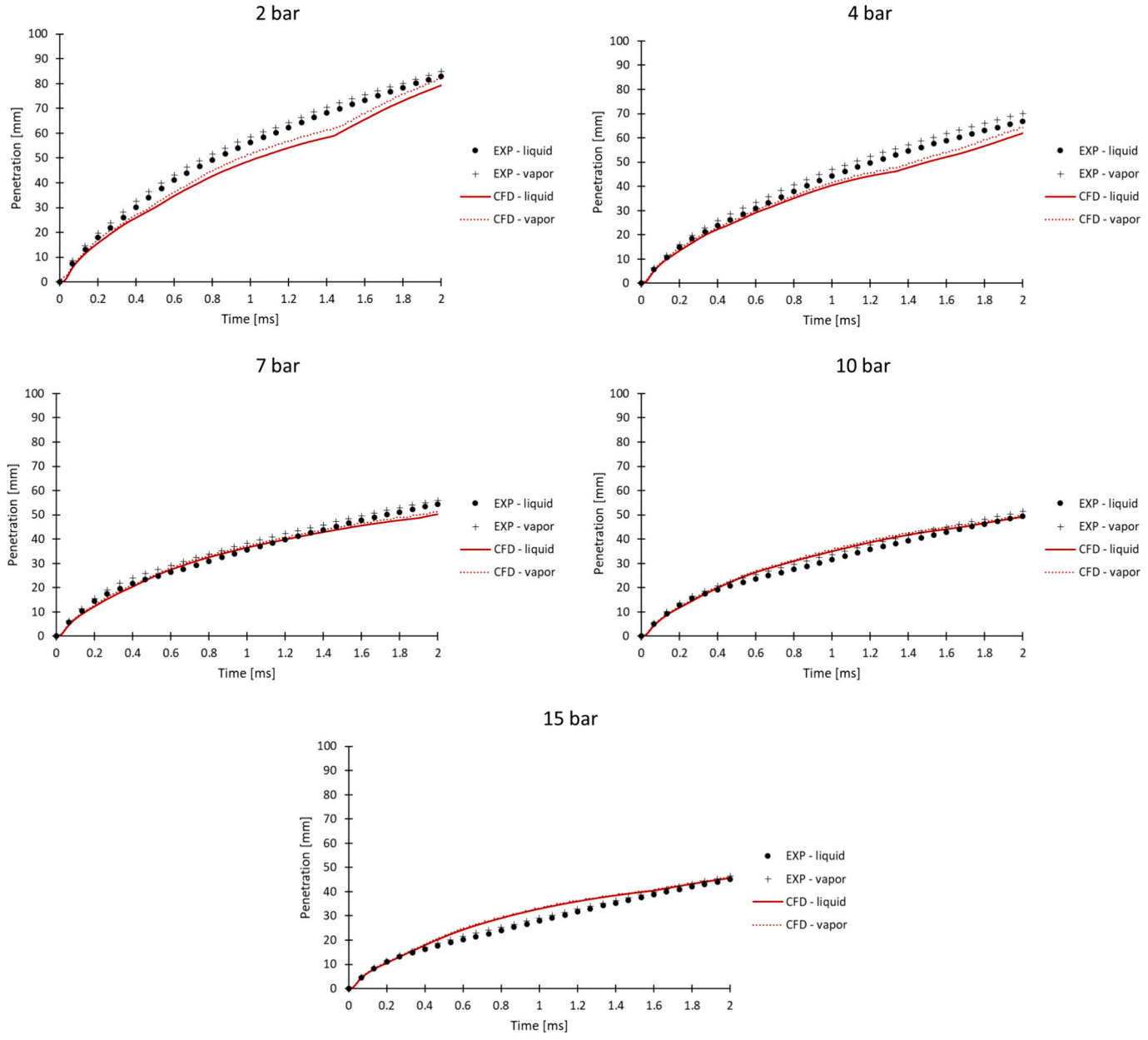

Fig. 5. Comparison between experiments and simulation in terms of liquid and vapor penetration.

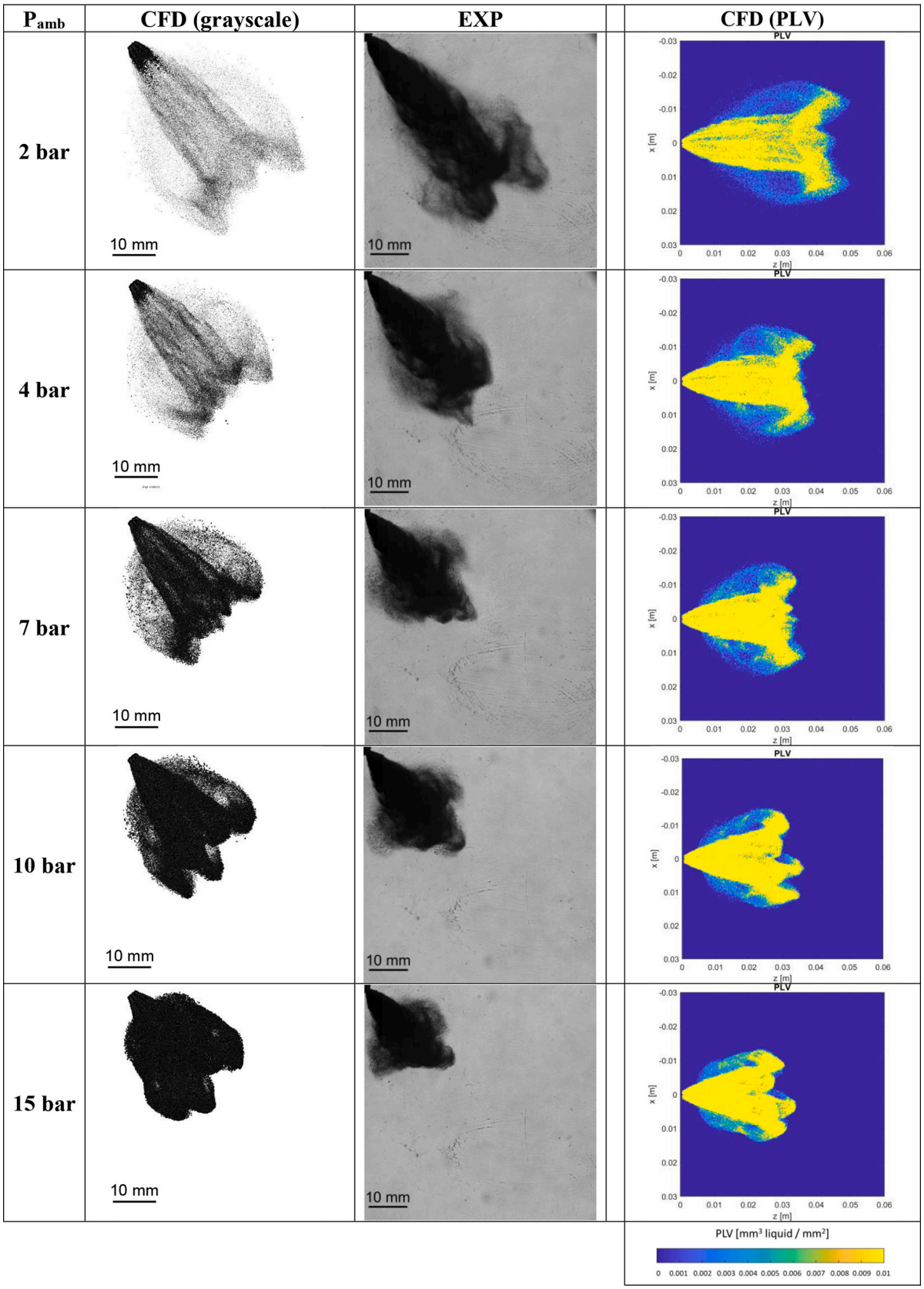

Fig. 6. Comparison between experiments and simulations in terms of spray morphology at $t = 1$ ms ASOI.

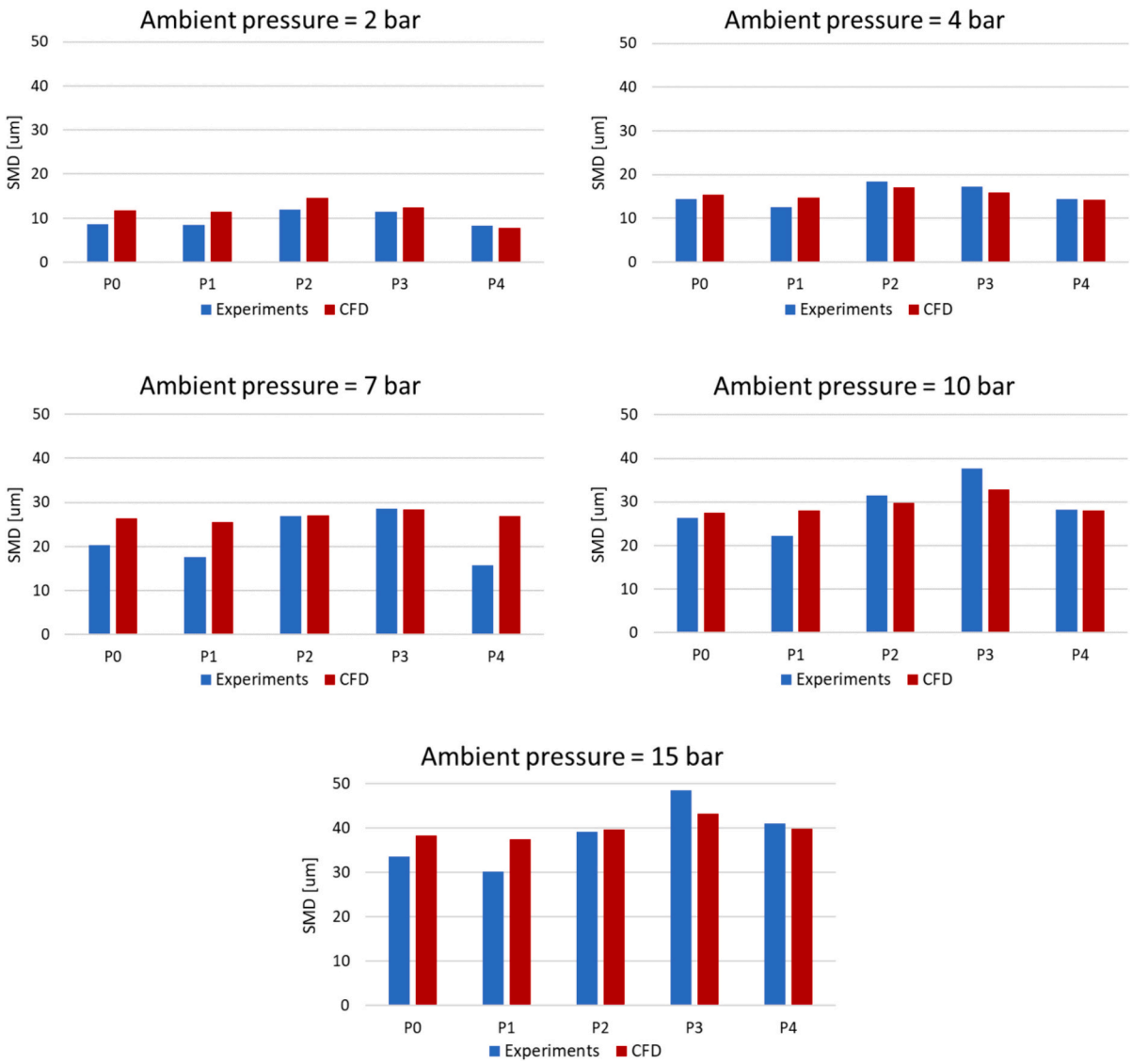

Fig. 7. Comparison between experiments and simulation in terms of local SMD.

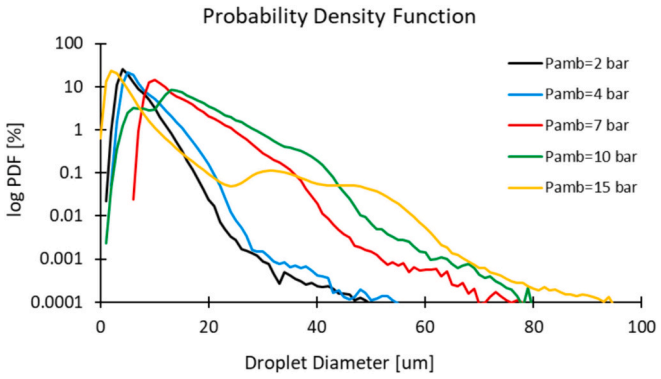

Fig. 8. Comparison between global PDF of parcel diameter based on number density.

high result quality.

Regarding thermal aspects, the Frossling correlation [50] is used to model phase change due to evaporation. Additionally, flash boiling requires particular attention since its occurrence is easily observed with ammonia due to its high saturation pressure. Here, flash boiling is modeled following Price et al. [28] which considers superheat evaporation. Two droplet mass transfer rates are considered, a subcooled term dM_{sc}/dt and a superheat term dM_{sh}/dt. The calculation for the subcooled term is expressed as follows

$$\frac{dM_{sc}}{dt} = 4\pi R_d^2 P_\infty \frac{Sh\, D_i}{T_f\, R_f\, 2R_d}\, ln\left(\frac{P_\infty - P_v}{P_\infty - P_s}\right) \tag{7}$$

where R_d is the drop radius, P_∞ the cell pressure, Sh the Sherwood number, D_i the binary diffusivity, T_f the vapor film temperature, R_f the vapor film specific gas constant, P_v the partial vapor pressure of the drop species, and P_s the saturation pressure of the species. The liquid film properties are evaluated using the one-third rule. The superheat term is expressed as follows

$$\frac{dM_{sh}}{dt} = \frac{4\,\pi\, R_d^2\, \alpha\, (T - T_b)}{H_L} \tag{8}$$

where H_L is the latent heat of evaporation of the liquid, T the fuel temperature, and T_b the boiling temperature. The empirical relation proposed by Adachi et al. [51] is used to determine the heat transfer coefficient α between liquid and air.

The rate of change of drop mass computed by Eqs. (7) and (8) are not

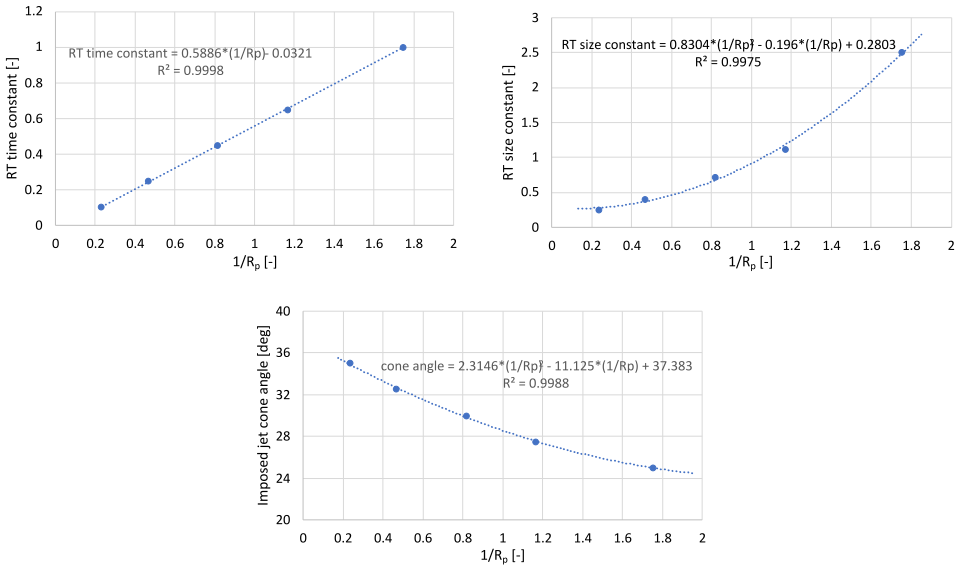

Fig. 9. Correlations for RT time constant, RT size constant, and neat-exit jet cone angle.

mutually exclusive, but both act simultaneously on the drop, contributing with their evaporative or condensing effect, depending on local thermodynamic conditions (pressures and temperatures). The total evaporation rate dM_t/dt is calculated as the sum

$$\frac{dM_t}{dt} = \frac{dM_{sc}}{dt} + \frac{dM_{sh}}{dt} \tag{9}$$

The reduction of drop size based on flash boiling is calculated from the mass rate of change using the droplet diameter reduction sub-model as follows

$$\frac{dr_d}{dt} = \frac{1}{4\pi\rho r_d^2}\frac{dM_t}{dt} \tag{10}$$

Drop temperature is then calculated from the following energy balance

$$m_d c_p \frac{dT_d}{dt} = -4\,\pi\,R_d^2\,\alpha(T_d - T) + H_L\frac{dM_t}{dt} \tag{11}$$

The following equation is used to model the vapor mass diffusivity

$$\rho_{gas} D = 1.293\,D_0\left(T_{gas}/273\right)^{n_0-1} \tag{12}$$

where $D_0 = 2.8 \times 10^{-5}$ and $n_0 = 2.75$ are properly representative values for ammonia. Additionally, vapor pressure, liquid density and specific heat data are needed. These values are provided as tabulated properties as a function of liquid temperature [26], and are shown in in Fig. 2.

Five cases are simulated, whose details are reported in Table 2. Fuel is injected at 120 bar and 293 K, and ambient temperature is set at 293 K. The ambient pressure varies from 2 to 15 bar. The superheat degree, measured by the pressure ratio R_p, is reported for each case in order to characterize the flash boiling intensity. R_p is defined as the ratio between the saturation vapor pressure corresponding to the temperature of the injected fuel and the ambient pressure, i.e., $R_p = P_v(T_{fuel})/P_a$. When $R_p < 1.0$ flash boiling is not supposed to occur, while cases with $R_p > 1$ are characterized by the presence of flash boiling. The case with 2 bar ambient pressure ($R_p = 4.285$) corresponds to a strong flash boiling situation.

The jet orientation and the near-exit cone angle are crucial parameters to assign as boundary conditions. In this study, the plume directions remain consistent for both flashing and non-flashing scenarios, utilizing the nominal directions as previously documented in Table 1 and visually depicted in Fig. 1.b. On the other hand, the enhanced atomization level produced by micro-explosions under flash boiling conditions is reproduced by adjusting the two RT breakup model constants and simultaneously enlarging the near-exit jet cone angle as a function of R_p. The details will be presented and discussed in depth in the Results section.

The injected mass per shot was measured experimentally, for a fixed injection duration of 3.9 μs and a fixed injection pressure of 120 bar. However, the injection rate shape is not available, so, it has been prescribed by analogy with the well-known ECN Spray G [52]. The mass flow rate curves for each back-pressure are shown in Fig. 3. A discharge coefficient $C_d = 0.69$ was found experimentally and used as input for the CFD simulation, coupled with an assumed velocity coefficient $C_v = 1$. The steady-state flow rate decreases as the difference between the injection pressure and the ambient pressure reduces.

2.2. Experimental spray imaging and droplet size data

Experimental investigations of liquid ammonia injections are conducted in a constant volume vessel. The details of the spray rig setup has been reported in [18], and only a summary is provided here. Throughout the experimental campaign, ammonia is maintained at 20 °C and compressed to 120 bar using pressurized helium. The air temperature inside the chamber is controlled and set to 20 °C, while the ambient pressure is regulated to obtain various levels of back-pressure.

The liquid and vapor spray boundaries are tracked based on the Schlieren technique. A collection of 100 raw images is used for calculating an ensemble average of the experimental results at each timing. The high sensitivity to refractive index gradients allows for the detection of the line-of-sight boundary between vaporized fuel and ambient gases [53]. The sensitivity is influenced by light intensity and can be modified using a diaphragm positioned in front of the camera; in particular, the sensitivity increases using a small diaphragm opening. From these averaged images, macroscopic parameters, like liquid and vapor penetrations, have been determined.

For each test condition, local values of the droplet Sauter Mean Diameter (SMD) are measured using a Malvern analyzer. Five distinct locations within the spray are considered, as displayed in Fig. 4. The technique provides a line-of-sight average of the droplet diameter for each position. The results of this campaign have been presented in our recent works [26,27] and are used here for model validation.

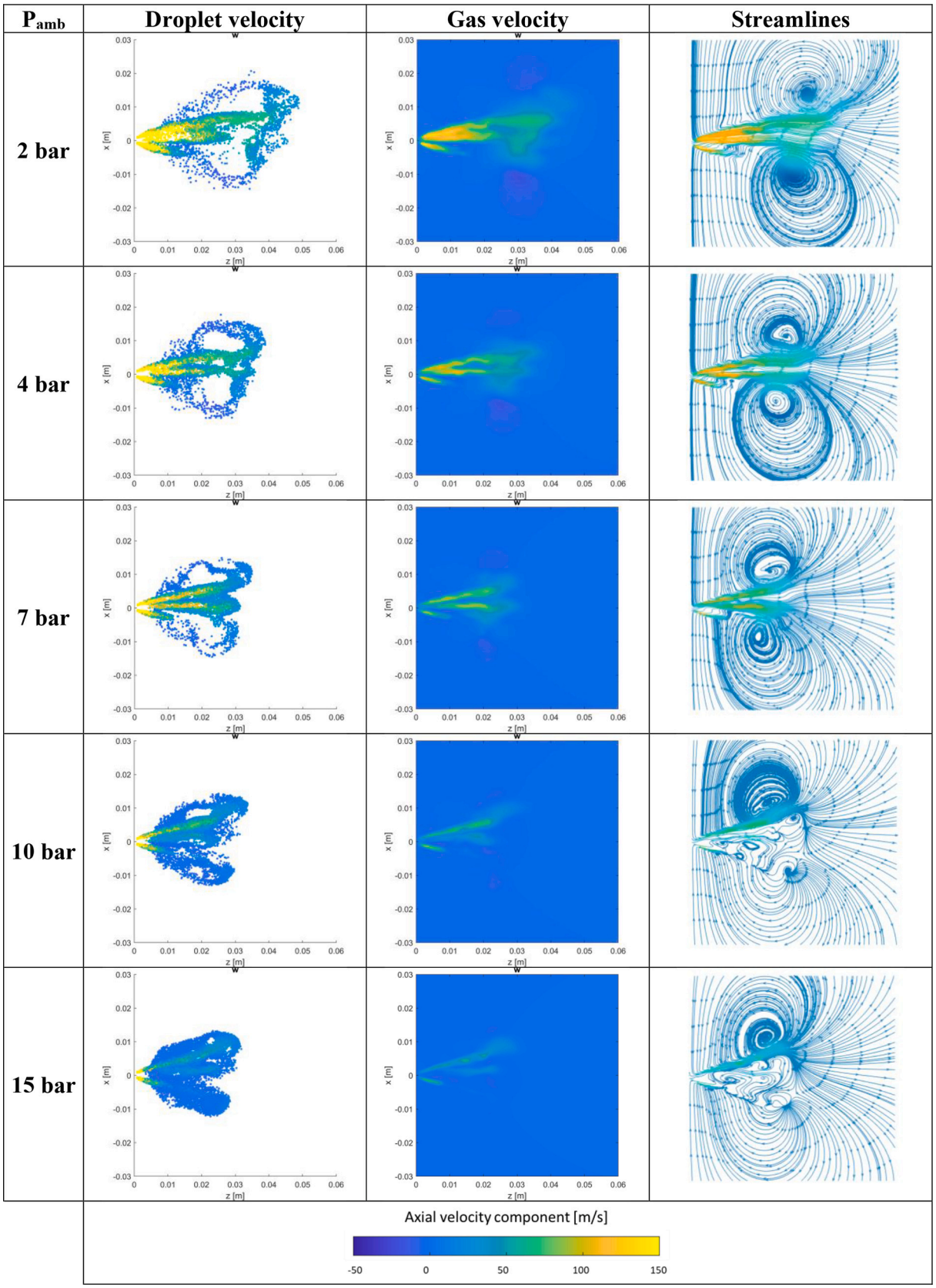

Fig. 10. Comparison among droplet, gas axial velocity component and flow streamlines colored with gas axial velocity, at 1 ms ASOI.

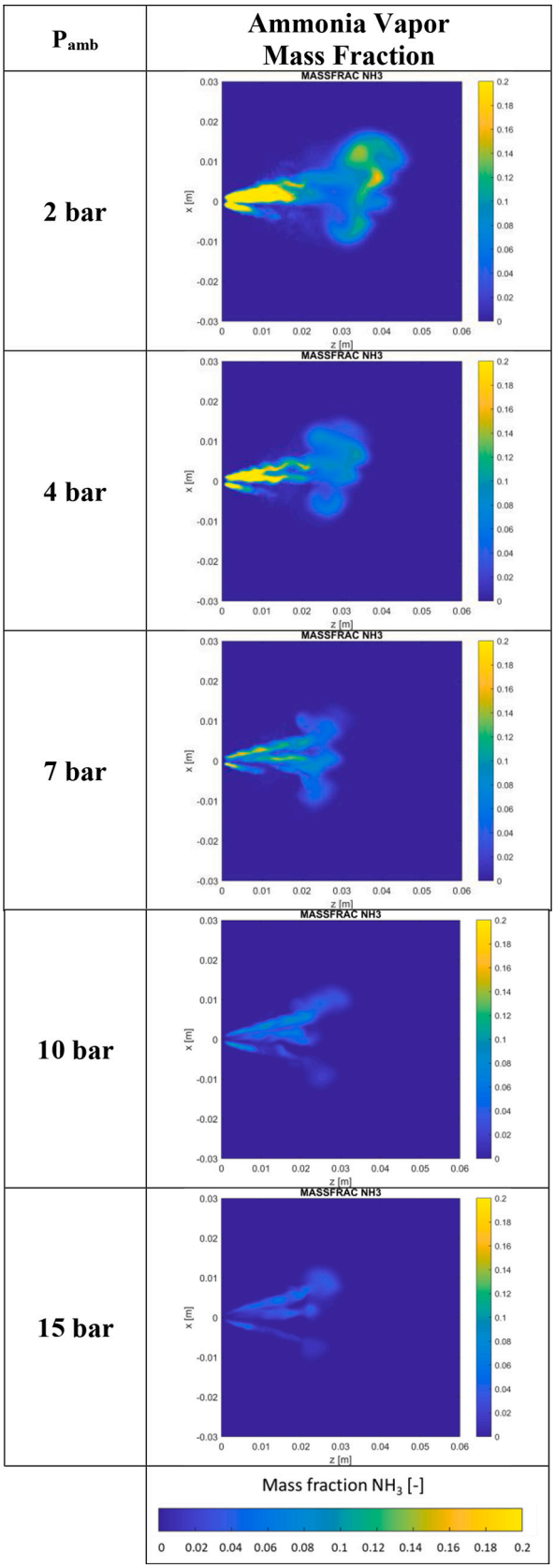

Fig. 11. Comparison between vapor ammonia mass fraction in a slice passing through the injector axis, at 1 ms ASOI, in the color range between 0 and 0.2.

3. Results and discussion

3.1. Spray atomization correlations and validation

The result analysis begins with the main macroscopic characteristic considered within the spray research framework, i.e., spray penetration. A comparison of liquid (solid lines) and vapor (dotted lines) penetrations are shown in Fig. 5 against experimental imaging data. The comparison clearly shows the good agreement between simulations and experiments in terms of spray tip penetration. To be more critical, a slight under-prediction is shown for the two lowest ambient pressure conditions, where the flash boiling phenomenon is more intense. Furthermore, since the injector is a multi-hole, slowing down or acceleration of the individual jets may occur due to localized fluid dynamic phenomena. This justifies the presence of particular trends in the calculation of CFD global penetration, evident for the 2 bar case after 1.4 ms aSOI. However, almost equal liquid and vapor spray tip penetrations are depicted by the CFD models for all conditions, in line with the experimental trends.

In addition to an accurate spray tip penetration, a correct spray morphology prediction is essential. Fig. 6 shows a comparison of the spray shape at 1 ms ASOI, CFD grayscale results are on the left column and experimental images on the middle one. Concerning numerical results, the droplet dimension is scaled with the droplet diameter, and also a grayscale is applied proportional to the diameters themselves. This type of visualization is meant only to produce a spray image which is visually comparable to the experimental liquid ones obtained by the high-speed Schlieren. Fig. 6 also shows projected liquid volume (PLV) results on the right column. These data are more quantitative, as they represent the line-of-sight integral of the volume occupied by the liquid phase. Overall, by considering grayscale or PLV post-processing results, the predicted spray morphology shows a fair agreement with the experimental images, especially for the two lowest ambient pressure conditions. It must be noted that the jet cone angle plays a significant role and contributes significantly to the global spray morphology obtained by the simulations [27]. Using too low cone angle values the predicted jets would be completely separated. Considering the experimental images, one can clearly observe that plume-to-plume interaction is present. Therefore, appropriate values should be used. In this work, a specific calibration of this model parameter has been done, modifying the jet cone angle progressively as the ambient pressure increases. Larger values are needed at low back-pressures, and these have been specified as a function of R_p, as will be discussed later. In this way, compared to our preliminary work [27], improved predictions of the spray morphology and spray tip penetration have been obtained.

Next, local results are analyzed. In this regard, the local SMD comparison is shown in Fig. 7, with experimental results reported in blue and CFD results in red. As previously mentioned, to achieve such predictions the coefficients of the RT breakup model had to be adapted, spanning from the flash boiling regime to the non-flashing one in order to reproduce experimental values. This suggests that capturing spray local details across all the regimes with a single model is still challenging, especially with a new fuel such as ammonia. Nevertheless, analyzing the five positions, trend-wise predictions indicate larger droplets on the external locations (pos. 2 and 3), as observed in the measurements. Globally, the calibrated CFD model provides accurate local SMD predictions for all the ambient conditions studied and in all the locations considered, strengthening the validation of the model set-up.

Fig. 8 shows a comparison of the global PDFs (probability density function) of droplet diameter in terms of particle number, predicted for each analyzed case. These distributions are based on the number of droplets in each class of diameter. Results are consistent with the local SMD values shown in Fig. 7. All distributions have a main peak on the low-end side of the chart, because the number of small droplets is very large here, but their mass is quite small. SMD values which are weighted on the mass (or volume) are much larger. As an example, the 15 bar back-pressure shows an evident hump in the range of 40–50 μm, and the

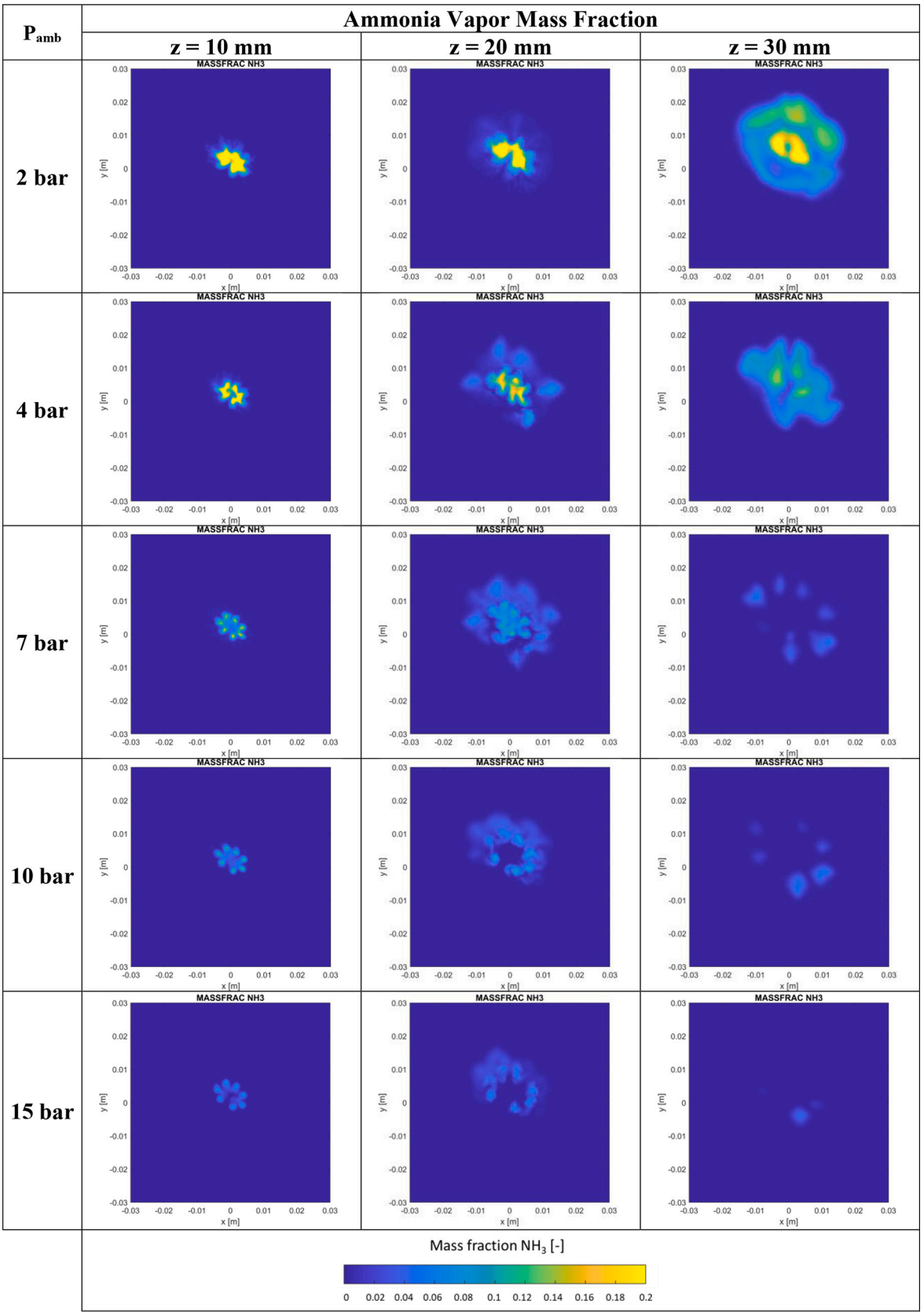

Fig. 12. Comparison among ammonia vapor mass fractions, within the gas phase, at 10, 20 and 30 mm distance from the injector position, at 1 ms ASOI, in the range between 0 and 0.2.

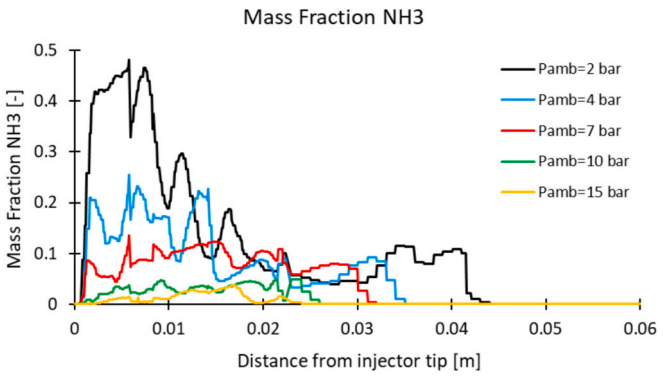

Fig. 13. Comparison among ammonia vapor mass fractions, within the gas phase, along the injector axis, at 1 ms ASOI.

SMD is in fact in that range. The two flashing cases show similar trends among each other, in particular the 2 bar case produces a PDF shifted towards smaller diameters compared to the 4 bar case. Similarities are also visible for the 7 and 10 bar cases, which have R_p values around unity. The 15 bar case, instead, shows a different behavior characterized by 2 distinct peaks, as noted earlier.

In summary, the results presented so far, concerning validated global and local spray features, have been obtained after a proper calibration of the near-exit jet cone angle (θ) and of the RT breakup constants (C_{RT},C_I). This activity led to the development of three correlations for the near-exit cone angle, the RT time constant and RT size constant, as shown in Fig. 9 and reported below

$$\theta = \frac{2.3146}{R_p^2} - \frac{11.125}{R_p} + 37.383\ [deg] \tag{13}$$

$$C_{RT} = \frac{0.8304}{R_p^2} - \frac{0.196}{R_p} + 0.2803 \tag{14}$$

$$C_I = \frac{0.5886}{R_p} - 0.0321 \tag{15}$$

These correlations are the result of polynomial regression fits based on the values successfully utilized in the simulations, as a function of the inverse of pressure ratio (R_p) from the different operating conditions. The results of the mathematical fits have an R-squared values in excess of 0.99, exhibiting excellent accuracy. The RT time constant C_I correlation exhibits a linearly increasing trend as the ambient pressure increases (recalling that $p_a = p_v(T_{fuel})/R_p$), while the RT size constant C_{RT} correlation displays a variable slope, which tends to change from the superheated to the subcooled regimes. The cone angle variation is also nonlinear, exhibiting a steeper change as superheat increases. The chosen cone angle variation is sufficient to reproduce the jet-to-jet interaction in the near field, which controls the spray collapse, as also reported by Liu et al. [54]. No changes in the initial jet directions have been attempted, to further control spray collapse occurrence. Jet initial directions have been kept fixed and equal to the values reported in Table 1. This agrees with near-nozzle closeup views of flashing and non-flashing sprays, such as those reported by Moulai et al. in [55].

Lastly, it is noted that we selected R_p as the thermodynamic parameter for the proposed correlations because it is directly related to the difference in chemical potential, which is the fundamental quantity that represents the generalized driving force for phase transition, as discussed by Lamanna et al. [35]. Therefore, in an attempt to make the correlations robust, R_p seems the most appropriate choice, instead of RT or Jacob number, to measure the degree of departure from thermodynamic equilibrium in superheated conditions.

3.2. Analyses of gas and liquid phase features

The calibrated model has undoubtedly fair performance from both macroscopic and microscopic points of view, and it represents a trustworthy tool for ammonia spray simulations. Using this validated CFD model, many additional features of ammonia sprays can be analyzed, which are not available from the experiments. Firstly, flow dynamics are analyzed considering droplet and gas velocities as well as flow streamlines for the whole range of conditions studied. In Fig. 10 these quantities are depicted in a slice passing through the injector axis, at 1 ms ASOI, with the color bar ranging from −50 to 150 m/s. The snapshots clearly show the liquid-driven dynamics of the ammonia jets, with high-speed drops that drag the gas in the corresponding region of space at slightly lower speeds. Additionally, as ambient pressure is increased the velocity is reduced, in line with the shorter tip penetration. It is worth pointing out that the shorter jet on the lower side of each slice (negative x direction) is due to the non-symmetric spray pattern, or, in other words, the slice does not cut any jet on the lower side of the image.

Regarding the flow streamlines, a characteristic pattern of a free jet injected into a large chamber is shown. The gas entrainment pattern is perpendicular to the spray axis as the flow approaches the spray radial limit, then it turns sharply and becomes almost axial inside the spray [56]. Moreover, two circular flow vortexes, almost symmetrical, are visible at the spray radial limit in the vicinity of the jet tip for ambient pressures lower than 10 bar. These gas flow features are the consequence of the air entrainment, as reflected by the homologous liquid zones exhibiting a lack of droplet velocity. However, the recirculation pattern at the bottom of the slice vanishes for the two highest ambient pressure conditions, i.e., 10 and 15 bar. At these two conditions, the superheat degree R_p is lower than 1.0, and therefore, the flash boiling phenomenon does not occur generating an asymmetrical air entrainment flow.

Ammonia vapor mass fraction can be of interest for analyzing the spray formation process. Fig. 11 shows the ammonia vapor mass fraction in a slice passing through the injector axis, at 1 ms ASOI, with the color bar ranging from 0 to 0.2. Moreover, in Fig. 12 a comparison among vapor mass fraction distributions at 10, 20 and 30 mm distance from the nozzle is shown, at 1 ms ASOI. A marked difference can be noted between the flashing and non-flashing regimes: for the extreme flashing case (2 bar) there is a high concentration of ammonia vapor which exceeds 20% mass fraction. This effect decreases moving towards higher back pressures: for the cases at 4 and 7 bar the peak concentration of ammonia vapor is around 15–20%. For the non-flashing cases (10 and 15 bar) the quantity of ammonia vapor is much smaller since it reaches maximum values around 5%. This difference in ammonia vapor behavior is due to the different regimes analyzed. Basically, ammonia vapor is created due to flash boiling phenomenon, and this is the reason for being present in a greater amount for the strong flashing case. In addition, the jet collapse is well visible in Fig. 12 at low ambient pressures, in particular for the external jets whose imprints are merged. This effect is evident for the cases at 2, 4 and 7 bar, while jets are completely separated for the cases at 10 and 15 bar.

The same behavior can also be seen from the plot in Fig. 13, where the mass fraction of ammonia vapor along the injector axis is represented at 1 ms ASOI. The quantity of ammonia vapor decreases as the ambient pressure increases, i.e., moving from extreme flashing (2 bar case in black) to evaporative cases (10 bar in green and 15 bar in yellow). For the flash boiling cases, (2 bar case) achieves twice the ammonia mass fraction of the 4 bar case. On the contrary, the cases under pure evaporative conditions (10 and 15 bar) have a similar trend between them, consistently with the fact that phase change is only controlled the ambient temperature which is the same. Furthermore, the effect of the ambient pressure on the spray penetration can be seen again: the penetration of the ammonia vapor decreases as the chamber pressure increases.

Fig. 14 shows a comparison of the droplet and gas temperatures at 1 ms ASOI. Droplet and gas temperatures are displayed in the range

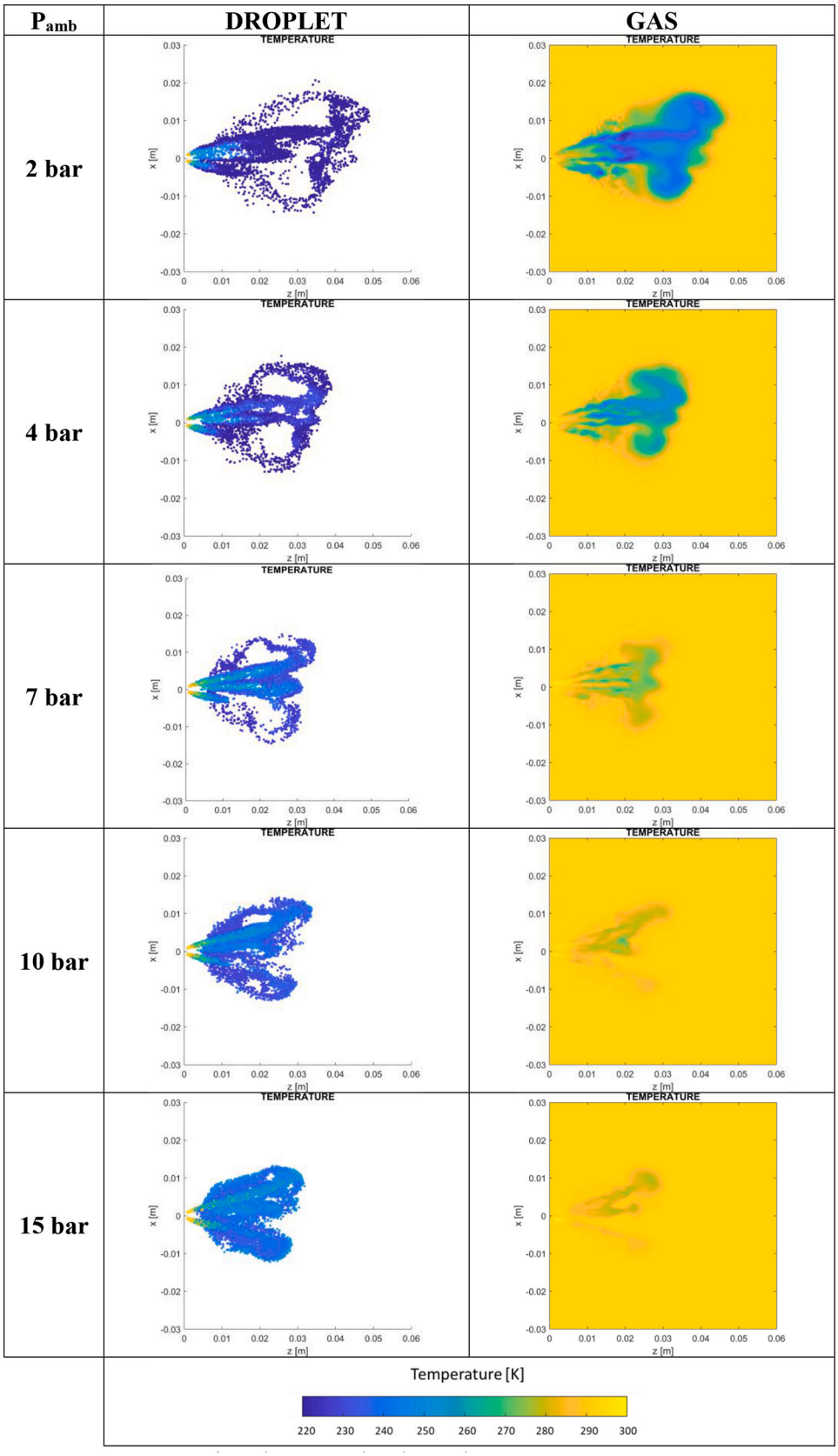

Fig. 14. Comparison between droplet and gas temperature, at 1 ms ASOI.

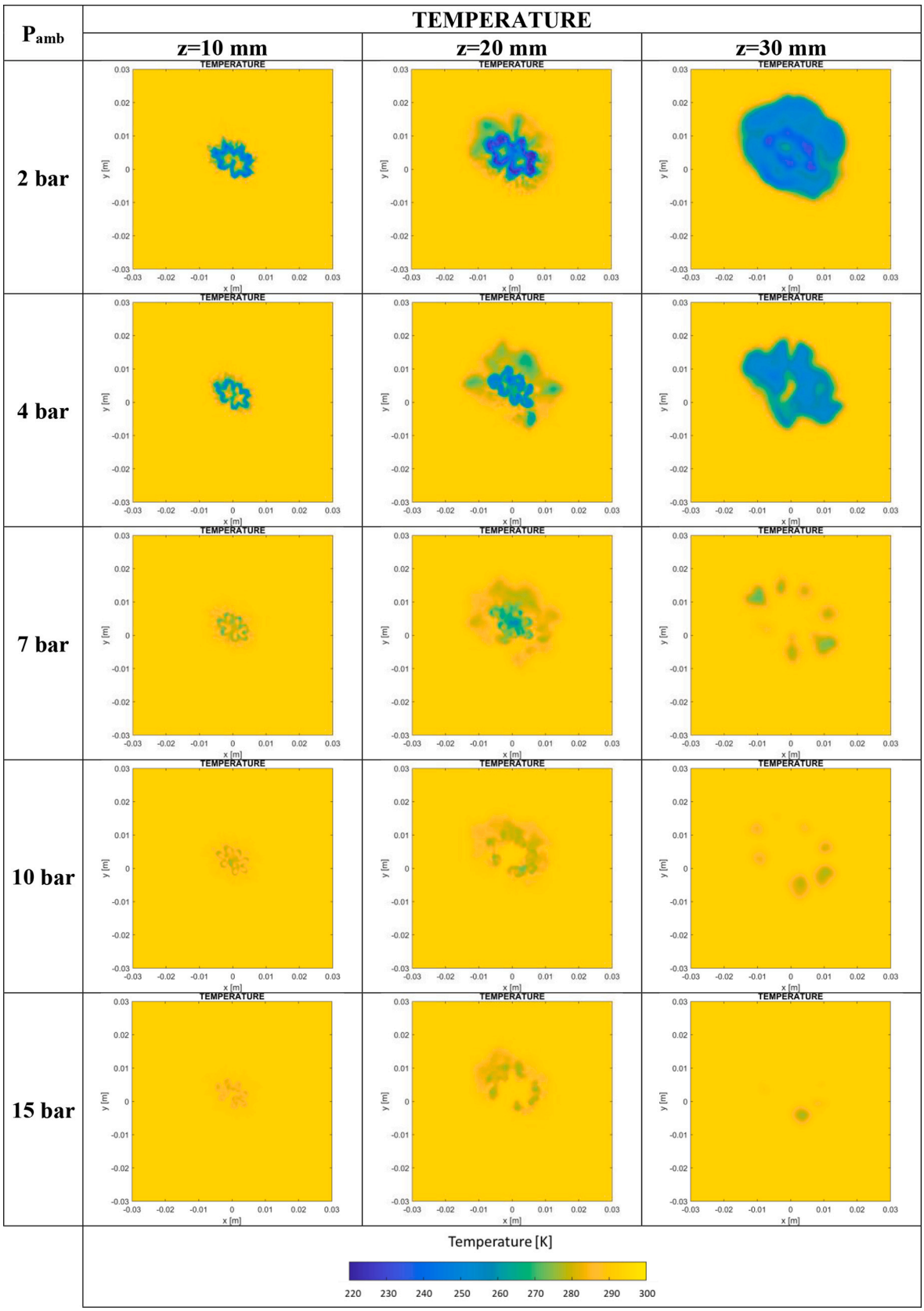

Fig. 15. Comparison among gas temperature distributions at 10, 20 and 30 mm distance from the injector position, at 1 ms ASOI.

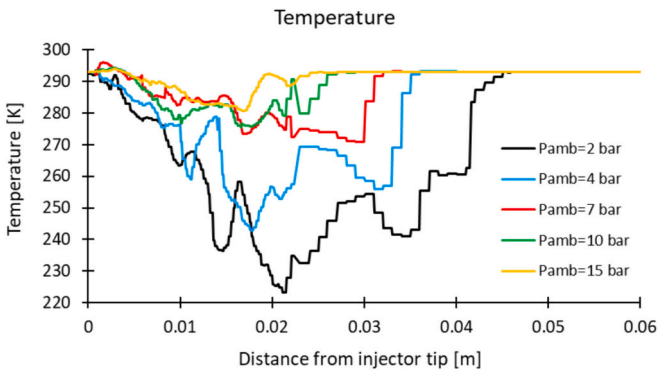

Fig. 16. Comparison among gas temperature profiles along the injector axis, at 1 ms ASOI.

between 220 and 300 K, noting that the gas temperature is represented in a slice passing through the injector axis, while droplet data are scattered because refers to particles belonging to a thin slice. The far field gas temperature of the chamber is 293 K as the liquid ammonia injection temperature. To corroborate the analysis, in Fig. 15 a comparison among ammonia temperature contours at 10, 20 and 30 mm distance from the nozzle is shown, at 1 ms ASOI. Gas temperatures are displayed in the range from 220 to 300 K, in a similar fashion to the previous figure.

It is also worth recalling that ammonia has a large heat of vaporization compared to hydrocarbon fuels. As an example, at 293 K ammonia heat of vaporization is 1187 kJ/kg, while isooctane has a value of 310 kJ/kg. Consequently, strong cooling effects are observed with ammonia, especially under flash-boiling conditions. The predicted temperatures have distinct features for the two regimes. Under non-flashing conditions, droplets are in subcooled regime at 10 and 15 bar. Vaporization causes the particles to cool down to about 270 K, while the surrounding gas cools by a few degrees, from 293 K down to about 280 K. The cooling effect is mild but considering that liquid and gas are introduced at room temperature, the effects are not negligible.

Moving to flash boiling conditions (cases at 4 and 7 bar) the temperature decrease is more evident for both droplet and gas phases: particles cool down to about 240 K and the surrounding gas cools to about 260–270 K. For the extreme flashing case at 2 bar, flash boiling causes a strong thermal imbalance due to the faster phase change of liquid ammonia to vapor. Droplets reach temperatures of 220 K a few millimeters after the injection point, and correspondingly the temperature of the surrounding gas cools down by about 40 K with respect to the initial condition, to about 250 K. This can be interpreted considering that ammonia saturation temperature at 2 bar is 255 K, so at equilibrium the liquid and the surrounding vapor tend towards this temperature. In addition to that, local dynamics plays a role. Local conditions can go below the average ambient level, and the fast process can also lead to a certain degree of subcooling during the phase change, with undershooting below its equilibrium saturation temperature. These aspects can justify the low temperature levels recorded locally for the liquid ammonia, cf., for example, minimum temperatures of about 220–230 K in some locations.

Fig. 16 shows the comparison of gas temperature along the injector axis at 1 ms ASOI. The gas temperature follows the trends already discussed, with a significant cooling for flash boiling cases. The thermal imbalance compared to the ambient condition ($T = 293$ K) increases as the superheat degree R_p increases. Temperature predictions for two evaporating cases show a similar trend.

4. Conclusions

In this work, the assessment of proposed primary breakup models for Lagrangian simulations of ammonia sprays in flash boiling condition is presented and compared with experimental data.

- A predictive calibrated CFD Lagrangian framework has been defined for ammonia multi-hole sprays.
- Global spray parameters, such as liquid and vapor tip penetration and spray morphology, are relatively easy to reproduce, while local characteristics and atomization levels require a specific adaptation of the atomization parameters.
- Using the KH-RT breakup model, correlations for RT time and size constants have been established, along with a correlation for the near-exit cone angle. The RT time constant correlation shows an increasing linear trend as the ambient pressure increases, while the RT size constant correlation indicates two linear trends whose slope changes in the vicinity of ammonia vapor pressure at 293 K (8.57 bar). Cone angle monotonically increases with R_p.
- The trends in droplet and gas temperatures predicted by the CFD model highlight the strong cooling effects under flash boiling cases due to the large heat of vaporization.

Nomenclature

ASOI	After Start of Injection
CFD	Computational Fluid Dynamics
ECN	Engine Combustion Network
GDI	Gasoline Direct Injector
KH	Kelvin-Helmholtz
PDF	Probability Density Function
PLV	Projected Liquid Volume
RT	Rayleigh-Taylor
SMD	Sauter Mean Diameter
RANS	Reynolds-Averaged Navier-Stokes

CRediT authorship contribution statement

J. Zembi: Conceptualization, Formal analysis, Data curation, Methodology, Software, Validation, Investigation, Resources, Writing – original draft, Writing – review & editing, Visualization. **M. Battistoni:** Conceptualization, Formal analysis, Methodology, Software, Validation, Investigation, Resources, Writing – original draft, Writing – review & editing, Supervision, Funding acquisition. **A. Pandal:** Conceptualization, Formal analysis, Methodology, Software, Validation, Investigation, Writing – original draft, Writing – review & editing, Visualization. **R. Pelé:** Resources. **P. Brequigny:** Resources. **C. Hespel:** Resources. **C. Mounaïm-Rousselle:** Resources, Funding acquisition.

Declaration of competing interest

The authors declare that they have no known competing financial interests or personal relationships that could have appeared to influence the work reported in this paper.

Data availability

Data will be made available on request.

Acknowledgments

The University of Perugia authors acknowledge the partial support by the Italian PRIN 2020 funding source, within the H2ICE grant, project number 2020R92Y3Z.

The experimental data were obtained thanks to a PhD grant from labex CAPRYSSES - ANR-11-LABX-0006.

The computational resources provided by the Italian Cineca consortium under the Iscra Initiative - award IsC98_NH3-2022 - on the supercomputer Galileo100 are acknowledged.

References

[1] E.M. Sacramento, P. Carvalho, L.C. Lima, T. Veziroglu, Feasibility study for the transition towards a hydrogen economy: a case study in Brazil, Energy Policy 62 (2013) 3–9.

[2] P. Dimitriou, R. Javaid, A review of Ammonia as a compression ignition engine fuel, Int. J. Hydrog. Energy 45 (2020) 7098–7118.

[3] Y. Li, M. Bi, B. Li, Y. Zhou, L. Huang, W. Gao, Explosion Hazard evaluation of renewable hydrogen/Ammonia/air fuels, Energy 159 (2018) 252–263.

[4] H. Kobayashi, A. Hayakawa, K.D.K. Somarathne, E. Okafor, Science and technology of ammonia combustion, Proc. Combust. Inst. 37 (1) (2019) 109–133.

[5] A. Valera-Medina, H. Xiao, M. Owen-Jones, W.I.F. David, P.J. Bowen, Ammonia for power, Prog. Energy Combust. Sci. 69 (2018) 63–102.

[6] A. Valera-Medina, F. Amer-Hatem, A.K. Azad, I.C. Dedoussi, M. de Joannon, R. X. Fernandes, P. Glarborg, H. Hashemi, X. He, S. Mashruk, J. McGowan, C. Mounaim-Rouselle, A. Ortiz-Prado, A. Ortiz-Valera, I. Rossetti, B. Shu, M. Yehia, H. Xiao, M. Costa, Review on ammonia as a potential fuel: from synthesis to economics, Energy Fuel 35 (9) (2021) 6964–7029.

[7] E. Nadimi, G. Przybyła, T. Løvås, G. Peczkis, W. Adamczyk, Experimental and numerical study on direct injection of liquid ammonia and its injection timing in an ammonia-biodiesel dual injection engine, Energy 284 (2023) 1–10 (article number: 129301).

[8] A. Hayakawa, T. Goto, R. Mimoto, Y. Arakawa, T. Kudo, H. Kobayashi, Laminar burning velocity and markstein length of ammonia/air premixed flames at various pressures, Fuel 159 (2015) 98–106.

[9] M. Zhang, Z. An, X. Wei, J. Wang, Z. Huang, H. Tan, Emission analysis of the CH4/NH3/air co-firing fuels in a model combustor, Fuel 291 (2021) 120135.

[10] Z. An, M. Zhang, W. Zhang, R. Mao, X. Wei, J. Wang, Z. Huang, H. Tan, Emission prediction and analysis on CH4/NH3/air swirl flames with LES-FGM method, Fuel 304 (2021) 121370.

[11] T. Honzawa, R. Kai, A. Okada, A. Valera-Medina, P.J. Bowen, R. Kurose, Predictions of NO and CO emissions in ammonia/methane/air combustion by LES using a nonadiabatic flamelet generated manifold, Energy 186 (2019) 115771.

[12] M. Chang, J.H. Park, H.I. Kim, S. Park, Flash boiling macroscopic spray characteristics of multi-hole direct injection injectors with different hole arrangement, Appl. Therm. Eng. 170 (2020) 114969.

[13] M. Xu, Y. Zhang, W. Zeng, G. Zhang, M. Zhang, Flash boiling: easy and better way to generate ideal sprays than the high injection pressure, SAE Int. J. Fuels Lubr. 6 (2013) 137–148.

[14] M. Chang, Z. Lee, S. Park, S. Park, Characteristics of flash boiling and its effects on spray behavior in gasoline direct injection injectors: a review, Fuel 271 (2020) 117600.

[15] L. Wang, F. Wang, T. Fang, Flash boiling hollow cone spray from a GDI injector under different conditions, Int. J. Multiphase Flow 118 (2019) 50–63.

[16] E.C. Okafor, O. Kurata, H. Yamashita, T. Inoue, T. Tsujimura, N. Iki, A. Hayakawa, S. Ito, M. Uchida, H. Kobayashi, Liquid ammonia spray combustion in two stage micro gas turbine combustors at 0.25 MPa; relevance of combustion enhancement to flame stability and NOx control, Appl. Energy Combust. Sci. 7 (2021) 100038.

[17] E.C. Okafor, H. Yamashita, A. Hayakawa, K.K.A. Somarathne, T. Kudo, T. Tsujimura, M. Uchida, S. Ito, H. Kobayashi, Flame stability and emissions characteristics of liquid ammonia spray co-fired with methane in a single stage swirl combustor, Fuel 287 (2021) 119433.

[18] R. Pelé, C. Mounaïm-Rousselle, P. Bréquigny, C. Hespel, J. Bellettre, First study on ammonia spray characteristics with a current GDI engine injector, Fuels 2 (3) (2021) 253–271.

[19] S. Colson, H. Yamashita, K. Oku, K.D.K.A. Somarathne, T. Kudo, A. Hayakawa, H. Kobayashi, Study on the effect of injection temperature and nozzle geometry on the flashing transition of liquid ammonia spray, Fuel 348 (2023) 128612.

[20] A. Pandal, J.M. Pastor, J.M. García-Oliver, E. Baldwin, D.P. Schmidt, A consistent, scalable model for Eulerian spray modeling, Int. J. Multiphase Flow 83 (2016) 162–171.

[21] M. Battistoni, S. Som, C.F. Powell, Highly resolved Eulerian simulations of fuel spray transients in single and multi-hole injectors: nozzle flow and near-exit dynamics, Fuel 251 (2019) 709–729.

[22] J.M. Desantes, J.M. García-Oliver, J.M. Pastor, I. Olmeda, A. Pandal, B. Naud, LES Eulerian diffuse-interface modeling of fuel dense sprays near- and far-field, Int. J. Multiphase Flow 127 (2020) 103272.

[23] R. Torelli, S. Som, Y. Pei, Y. Zhang, M. Traver, Influence of fuel properties on internal nozzle flow development in a multi-hole diesel injector, Fuel 204 (2017) 171–184.

[24] S.K. Rachakonda, A. Paydarfar, D.P. Schmidt, Prediction of spray collapse in multi-hole gasoline direct-injection fuel injectors, Int. J. Engine Res. 20 (1) (2019) 18–33.

[25] Yanzhi Zhang, Xu Leilei, Yizi Zhu, Xu Shijie, Xue-Song Bai, Numerical study on liquid ammonia direct injection spray characteristics under engine-relevant conditions, Appl. Energy 334 (2023) 120680.

[26] A. Pandal, J. Zembi, M. Battistoni, C. Hespel, R. Pelé, P. Bréquigny, C. Mounaïm-Rousselle, GDI Ammonia Spray Numerical Simulation by Means of OpenFOAM, SAE Technical Paper, 2023, 2023-01-0311.

[27] J. Zembi, M. Battistoni, A. Pandal, C. Mounaïm-Rousselle, R. Pelé, P. Bréquigny, C. Hespel, Numerical study of Ammonia sprays with a GDI engine injector, J. Ammonia Energy 01 (2023), 059–073, ISSN 2752-7735.

[28] C. Price, A. Hamzehloo, P. Aleiferis, R. Richardson, An approach to modeling flash-boiling fuel sprays for direct-injection spark-ignition engines, Atomiz. Sprays 26 (12) (2016) 1197–1239, https://doi.org/10.1615/AtomizSpr.2016015807.

[29] J.R. Riznic, M. Ishii, Bubble number density and vapor generation in flashing flow, Int. J. Heat Mass Transf. 32 (10) (1989) 1821–1833.

[30] F. Duronio, S. Ranieri, A. Montanaro, L. Allocca, A. De Vita, ECN spray G injector: numerical modelling of flash-boiling breakup and spray collapse, Int. J. Multiphase Flow 145 (2021) 103817.

[31] L. Angelilli, P.P. Ciottoli, Galassi R. Malpica, M. Valorani, F.E. Hernandez-Perez, H. G. Im, A thermal flash-boiling model for secondary atomization of Lagrangian droplets, AIAA 2024-1637 (2024), https://doi.org/10.2514/6.2024-1637.

[32] J. Shin, S. Park, An ammonia flash break-up model based on bubble dynamics with force and energy analysis on droplet, Fuel 342 (2023) 127841.

[33] Y. Kitamura, H. Morimitsu, T. Takahashi, Critical superheat for flashing of superheated liquid jets, Ind. Eng. Chem. Fundam. 25 (1986) 206–211.

[34] E. Sher, T. Bar-Kohany, A. Rashkovan, Flash-boiling atomization, Prog. Energy Combust. Sci. 34 (2008) 417–439.

[35] G. Lamanna, H. Kamoun, B. Weigand, J. Steelant, Towards a unified treatment of fully flashing sprays, Int. J. Multiphase Flow 58 (2014) 168–184.

[36] X. Li, S. Wang, S. Yang, S. Qiu, Z. Sun, D.L.S. Hung, M. Xu, A review on the recent advances of flash boiling atomization and combustion applications, Prog. Energy Combust. Sci. 100 (2024) 101119.

[37] R.I. Issa, Solution of the implicitly discretised fluid flow equations by operator-splitting, J. Comput. Phys. 62 (1) (1986) 40–65, https://doi.org/10.1016/0021-9991(86)90099-9.

[38] K.J. Richards, P.K. Senecal, E. Pomraning, CONVERGE V.3.0 Documentation, Convergent Sciences Inc., 2020.

[39] P. Senecal, K. Richards, E. Pomraning, T. Yang, M.Z. Dai, R.M. McDavid, M. A. Patterson, S. Hou, T. Shethaji, A new parallel cut-cell Cartesian CFD code for rapid grid generation applied to in-cylinder diesel engine simulations, SAE Techn. Paper (2007), 2007-01-0159.

[40] Jesus Benajes, Jose M. Garcia-Oliver, Jose M. Pastor, Daiana De Leon-Ceriani, Unsteady Flamelet modeling study on OMEx-type fuels under engine combustion network spray A conditions, Fuel 331 (Part 2) (2023) 125458. ISSN 0016-2361, https://doi.org/10.1016/j.fuel.2022.125458.

[41] Leonardo Pachano, Xu Chao, Jose M. García-Oliver, Jose M. Pastor, Ricardo Novella, Prithwish Kundu, A two-equation soot-in-flamelet modeling approach applied under Spray A conditions, Combust. Flame 231 (2021) 111488. ISSN 0010-2180, https://doi.org/10.1016/j.combustflame.2021.111488.

[42] J. Zembi, M. Battistoni, S.K. Nambully, A. Pandal, C. Mehl, O. Colin, LES investigation of cycle-to-cycle variation in a SI optical access engine using TFM-AMR combustion model, Int. J. Engine Res. 23 (6) (2022) 1027–1046, https://doi.org/10.1177/14680874211005050.

[43] A. Pandal, B.M. Ningegowda, F.N.Z. Rahantamialisoa, J. Zembi, H.G. Im, M. Battistoni, Development of a drift-flux velocity closure for a coupled Σ-Y spray atomization model, Int. J. Multiphase Flow 141 (2021) 103691. ISSN 0301-9322, https://doi.org/10.1016/j.ijmultiphaseflow.2021.103691.

[44] J.K. Dukowitz, A particle-fluid numerical model for liquid sprays, J. Comput. Phys. 35 (1980) 229–253, https://doi.org/10.1016/0021-9991(80)90087-X.

[45] P.K. Senecal, E. Pomraning, K.J. Richards, S. Som, Grid-convergent spray models for internal combustion engine computational fluid dynamics simulations, ASME J. Energy Resour. Technol. 136 / (2014), https://doi.org/10.1115/1.4024861, 012204-1.

[46] R.D. Reitz, F.V. Bracco, Mechanisms of Breakup of Round Liquid Jets 3, Encyclopedia of Fluid Mechanics, Gulf Pub, NJ, 1986, pp. 233–249.

[47] T. Su, M. Patterson, R. Reitz, P. Farrell, Experimental and Numerical Studies of High Pressure Multiple Injection Sprays, SAE Technical Paper 960861, 1996, https://doi.org/10.4271/960861.

[48] P.J. O'Rourke, Collective Drop Effects on Vaporizing Liquid Sprays, Ph.D. Thesis, Princeton University, Princeton, NJ, United States, 1981.

[49] D.P. Schmidt, C.J. Rutland, A new droplet collision algorithm, J. Comput. Phys. 164 (1) (2000) 62–80, https://doi.org/10.1006/jcph.2000.6568.

[50] N. Frössling, Über die Verdunstung fallender Tropfen Gerlands Beitrag zur Geophysik 52, 1938, pp. 170–216.

[51] M. Adachi, D. Tanaka, Y. Hojyo, M. Al-Roub, J. Senda, H. Fujimoto, Measurement of fuel vapor concentration in flash boiling spray by infrared extinction/scattering technique, JSAE Rev. 17 (1996) 231–237, https://doi.org/10.1016/0389-4304(96)00025-2.

[52] https://ecn.sandia.gov. Accessed 2023-09-23.

[53] O. Nilaphai, C. Hespel, S. Chanchaona, C. Mounaïm-Rousselle, ILASS–Asia 2017 Oct. 18–21, 2017. Jeju, Korea.

[54] X. Liu, X. Yao, Z. Wang, C. Tang, Single hole ammonia spray macroscopic and microscopic characteristics at flare and transition flash boiling regions, Appl. Therm. Eng. 235 (2023) 121443, https://doi.org/10.1016/j.applthermaleng.2023.121443.

[55] M. Moulai, R. Grover, S. Parrish, D. Schmidt, "Internal and Near-Nozzle Flow in a Multi-Hole Gasoline Injector under Flashing and Non-Flashing Conditions," SAE Technical Paper 2015-01-0944, 2015, https://doi.org/10.4271/2015-01-0944.

[56] A. Pandal, J.M. García-Oliver, R. Novella, J.M. Pastor, A computational analysis of local flow for reacting diesel sprays by means of an Eulerian CFD model, Int. J. Multiphase Flow 99 (2018) 257–272, https://doi.org/10.1016/j.ijmultiphaseflow.2017.10.010.